Fjord-edge Graphene Nanoribbons with Site-Specific Nitrogen Substitution

Yolanda L. Li, Chih-Te Zee, Janice B. Lin, Victoria M. Basile, Mit Muni, Maria D. Flores, Julen Munárriz, Richard B. Kaner, Anastassia N. Alexandrova, K. N. Houk, Sarah H. Tolbert, and Yves Rubin*

Department of Chemistry and Biochemistry, University of California, Los Angeles, 607 Charles E. Young Dr. East, Los Angeles, California 90095–1567, United States

ABSTRACT: The synthesis of graphene nanoribbons (GNRs) that contain site-specifically substituted backbone heteroatoms is one of the essential goals that must be achieved in order to control the electronic properties of these next generation organic materials. We have exploited our recently reported solid-state topochemical polymerization/cyclization-aromatization strategy to convert the simple 1,4-bis(3-pyridyl)butadiynes **3a,b** into the fjord-edge nitrogen-doped graphene nanoribbon structures **1a,b** (fjord-edge N_2[8]GNRs). Structural assignments are confirmed by CP/MAS ^{13}C NMR, Raman, and XPS spectroscopy. The fjord-edge N_2[8]GNRs **1a,b** are promising precursors for the novel backbone nitrogen-substituted N_2[8]$_A$GNRs **2a,b**. Geometry and band calculations on N_2[8]$_A$GNR **2c** indicate that this class of nanoribbons should have unusual bonding topologies and metallicities.

■ INTRODUCTION

Graphene nanoribbons (GNRs) are expected to usher in the ultimate nanosizing of electronics[1,2,3,4] and sensors[5,6] for next generation devices. The electronic properties of GNRs can be exquisitely tuned by modification of their width, backbone, and edge structure.[1,7,8,9,10] In the last decade, both on-surface and in-solution bottom-up syntheses have achieved precise structural control over these benchmarks.[11,12,13,14,15] Early bottom-up syntheses have focused on GNRs with armchair[16,17,18,19] or zigzag[20] edges. More recently, intricate edge or interior configurations, such as chevron,[11,21,22,23] cove,[24,25,26] fjord[27] or holey,[28,29,30] have been obtained. These novel topologies significantly alter the electronic or magnetic properties of GNRs, as do atomically precise[31] substitutions of carbons with heteroatoms such as boron,[32,33] sulfur,[34,35] or nitrogen.[29,36,37] Crucially, site-specific doping at the GNR *backbone* produces a dramatic alteration of its electronics, making such structures the most desirable targets for synthesis.[31,38,39,40] Nitrogen doped GNRs are of particular interest as they produce p-doped materials.[23,36,37,41,42,43,44] Gratifyingly, creative ways to synthesize GNRs bearing novel edge or backbone structures are thriving to this day.[29,30,45]

Herein, we describe the synthesis of the first eight-atom wide, fjord-edge nitrogen-doped graphene nanoribbons **1a,b** (fjord-edge N_2[8]GNR; Figure 1). Fjord-edge N_2[8]GNRs **1a,b** were obtained in a facile two-step conversion starting from dipyridyl diynes **3a,b**. Photochemically-induced topochemical polymerization in the crystalline state afforded polydiacetylenes (PDAs) **4a,b**, which were thermally converted to GNRs **1a,b** without significant loss of the sidechains. The Hopf cyclization/aromatization from PDAs **4a,b** to GNRs **1a,b** was confirmed by cross-polarization magic angle spinning (CP/MAS) solid state ^{13}C NMR. X-ray photoelectron spectroscopy (XPS) revealed the pyridinic and amide bonding state of the nitrogen atoms. Raman spectroscopy further confirmed the structural integrity of the fjord-edge N_2[8]GNRs **1a,b**.

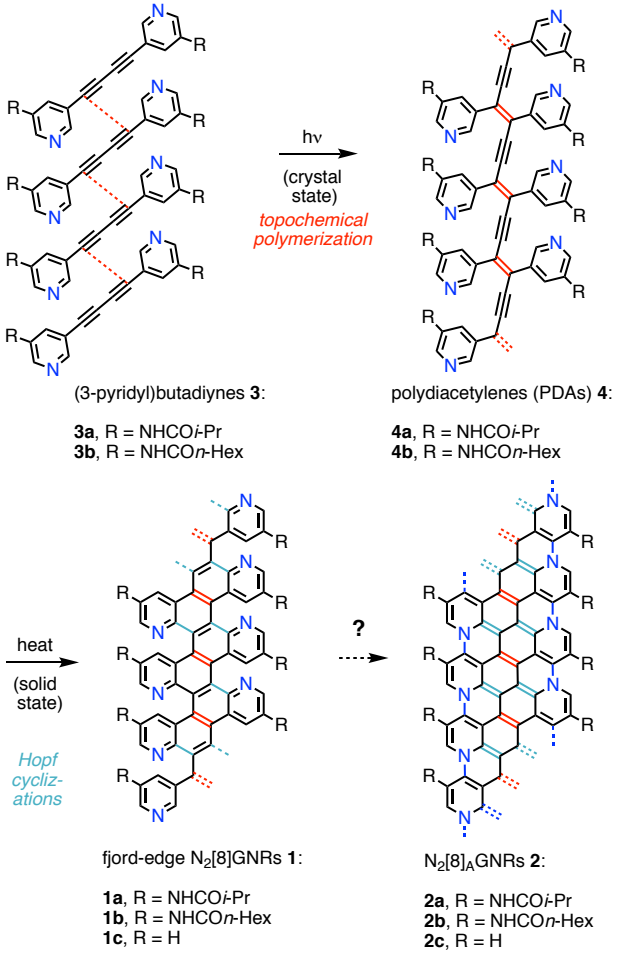

Figure 1. Synthesis of fjord-edge nitrogen-doped graphene nanoribbons (fjord-edge N_2[8]GNRs) **1a,b**.

■ RESULTS AND DISCUSSION

Diyne monomer synthesis: The topochemical polymerization of diynes requires suitable packing of the monomers in the crystal to trigger subsequent chain reactions.[46,47,48] Here, the dipyridyl diyne units of **3a,b,d** (Scheme 1) needed to have their diyne 1,4-carbons within van-der-Waals contact distance (~3.5 Å). This would promote the facile formation of intermolecular bonds, a process that often occurs under ambient light.[49,50] Although we synthesized several isomeric dipyridyl diyne systems,[51] only one series based on 3-amino-5-alkynylpyridine gave the polymerizable diynes **3a,b**. Accordingly, 3-amino-5-bromopyridine was coupled with trimethylsilylacetylene under Sonogashira conditions, followed by acylation of product **5** with the corresponding acid chlorides (Scheme 1, R = *i*-Pr, *n*-Hex, Me, respectively). Removal of the trimethylsilyl protecting group gave alkynyl amides **6a,b,d** in good to excellent yields. Oxidative coupling under the Hay conditions afforded diyne amides **3a,b,d** in good to high yields.

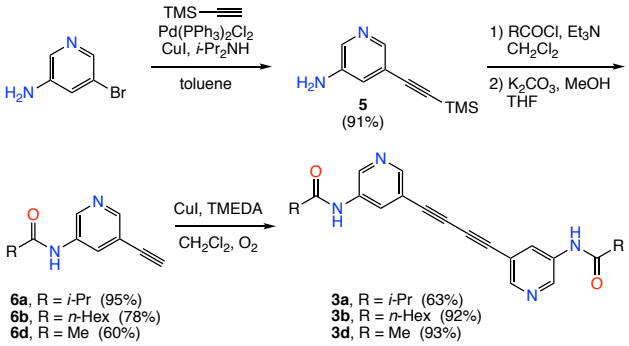

Scheme 1. Synthesis of 1,4-bis(3-pyridyl)butadiynes **3a,b,d**.

Crude diyne **3a** afforded single crystals after slow evaporation from methanol (Figures S28a,b).[51] X-ray diffraction at the Brookhaven Synchroton X-ray source (Figure S29) afforded a 1.0 Å resolution crystal structure (Figure 2 and Table S1).[51]

The crystal packing geometry for molecules of diyne **3a** validates the desired short C1–C4' distance of 3.45 Å (Figure 2a). The hydrogen bonds between the carbonyl oxygens and amide hydrogens have an optimal distance of 2.00 Å, guiding the assembly of diyne units in **3a** along the unit cell vector *a*. The relative strength of these intermolecular interactions is reflected in the crystal morphology and powder diffraction (Figures S28 and S30). To accommodate the H-bonding motif, the polymer growth axis exhibits a horizontal offset between each molecule, organizing the diynes into an optimal arrangement for topochemical polymerization (Figure 2b). Powder diffraction of **3b** displayed a similar packing arrangement to **3a** (Figure S31).

Both dipyridyl diynes **3a,b** easily polymerized to dipyridyl PDAs **4a,b** when subjected to UV light, as well as under ambient light, while diyne **3c** was unreactive. The polymerizations were carried out by irradiation of finely pulverized dispersions of the crystals in hexanes using a medium pressure Hanovia lamp (Pyrex filter), typically for 12 h, producing deep purple/black material. Dissolution of unreacted monomer from the polymerized crystals gave the pristine polydiacetylenes **4a,b** (18 and 4%, respectively) as fibrous powders after filtration. The one-step, low polymerization yield for **3b** appears to be inherent to this derivative, since repeated attempts to increase yields by using nanocrystalline material could not raise the conversion yield for this step.

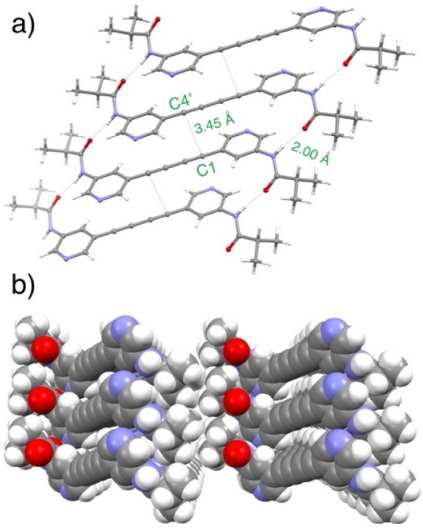

Figure 2. a) Crystal packing structure for diyne **3a** displaying the short C1-C4' distance directed by the C=O···H–N hydrogen-bonded network. b) View of **3a** down the H-bonding axis.

Conversion of PDAs 4a,b to GNRs 1a,b: Once PDAs **4a,b** became available, their conversion to GNRs **1a,b** could be studied by incremental heating under argon. Pyridyl GNRs **1a,b** form in a one-step concomitant Hopf cyclization and aromatization transformation to yield a fjord-edge GNR without significant loss of sidechains. This transformation was easily followed by CP/MAS ^{13}C solid state NMR, focusing on four distinct carbon signals corresponding to the four functional groups of interest: amide carbonyls (160–170 ppm), aromatic carbons (120–150 ppm), alkynyl carbons (~100 ppm), and amide sidechains (10–40 ppm, Figure 3b,c). As PDAs **4a,b** are heated under increasingly higher temperatures (1h each), the distinct ^{13}C NMR signals track an initial Hopf cyclization, as evidenced by the disappearance of the alkyne peak at temperatures between 300 and 350 °C, indicating that this cyclization occurs more readily than for our phenyl analogs.[50] This conversion is followed by aromatization to fjord-edge N_2[8]GNRs **1a** and **1b** between 350 and 400 °C, as revealed by the changes in aromatic signals between 110–155 ppm, which adopt an envelope having an underlying intensity ratio of 1:2:1 in both **1a** and **1b**, respectively. This ratio of intensities maps reasonably well with the calculated ^{13}C chemical shifts expected from a representative fjord-edge N_2[8]GNR segment (Table 1). Deconvolution of the experimental spectrum into seven individual ^{13}C signals of equal intensity and width affords the fitted values in Table 1. Furthermore, the convergence of both **4a** and **4b** to identical aromatic peak shapes indicates that they both likely undergo identical processes to form the same fjord-edge N_2[8]GNR core. Subsequent heating of **4a** and **4b** to temperatures as high as 400 °C shows no change in the ^{13}C CP/MAS spectra, suggesting that the fjord-edge N_2[8]GNR has fully formed at 330 °C and 360 °C starting from **4a** and **4b**, respectively. These milder temperatures prevent sidechain fragmentation, unlike in our previous work on [8]GNR, which required temperatures as high as 500 °C for full conversion.[50] Heating dipyridyl PDAs **4a,b** at temperatures higher than 400 °C (not shown) does not change the peak shape in the aromatic region, but shows gradual loss of the sidechains. Thus, it seems that full cyclization of fjord-edge N_2[8]GNRs **1a,b** to a N_2[8]$_A$GNRs **2a,b** does not occur under these conditions.

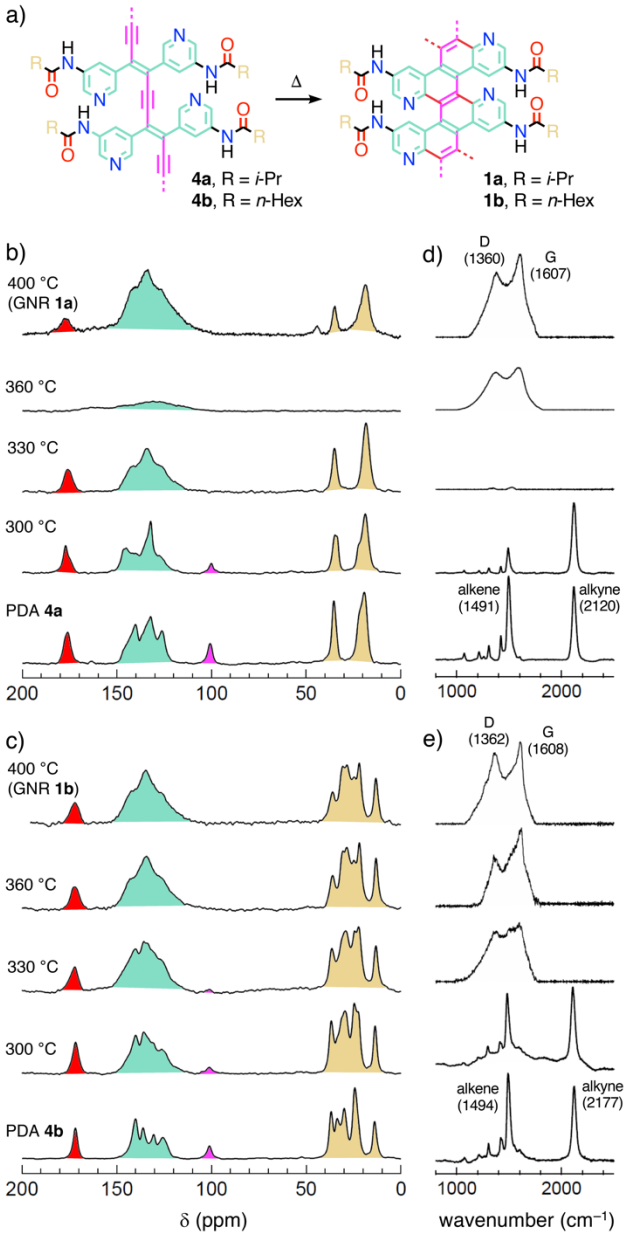

Figure 3. CP/MAS solid-state ^{13}C NMR and Raman spectra for the products obtained by heating PDAs **4a,b**. Each heating experiment was carried out for 1 h using a fresh sample of PDA. a) PDAs **4a,b** and GNRs **1a,b** are color-coded by chemical shift region to reflect spectral changes in b) and c). b) PDA **4a** conversion to fjord-edge N_2[8]GNR **1a,** and c) PDA **4b** conversion to fjord-edge N_2[8]GNR **1b**. The very broad weak signal for the sample heated at 360 °C in b) is due to an air-stable π-radical intermediate formed during heating.[52] Baseline-corrected Raman spectra for the conversion of d) PDA **4a** to fjord-edge N_2[8]GNR **1a**, and e) PDA **4b** to fjord-edge N_2[8]GNR **1b**.

The retention of sidechains during the aromatization process up to 400 °C positively affects the processability of these GNRs. As expected, the presence of the sidechains on fjord-edge N_2[8]GNRs **1a,b** increases their solubility: sonication in N-methyl-2-pyrrolidone (NMP) followed by filtration through a 0.2 μm Teflon membrane gives yellowish solutions (UV-vis, Figure S27).[51]

Table 1. Curve-Fitted Experimental CP/MAS ^{13}C NMR Spectrum of fjord-edge N_2[8]GNR 1a Compared to Calculated ^{13}C NMR Chemical Shifts for a Model Structure.[51] (a) Deconvolution Analysis[a] and (b) Structure of Calculated Model.

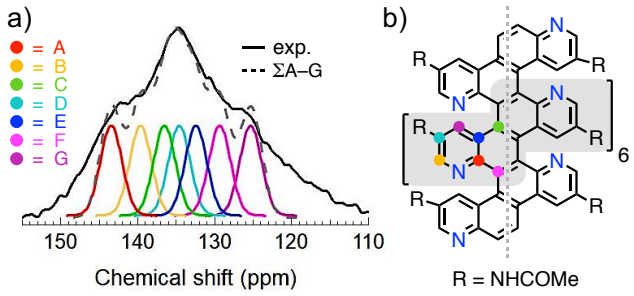

Carbon	A	B	C	D	E	F	G
Fitted δ	143.5	139.7	136.5	134.5	132.5	129.4	125.4
Calc. δ [b]	142.6	138.0	132.9	131.3	130.6	128.5	125.7

[a] The experimental CP/MAS ^{13}C NMR spectrum is plotted as a solid black line, the sum of the curve fits is the dashed line. [b] Average of the DFT calculated chemical shifts (GIAO/B3LYP//6-31G(d)) for each of the seven distinct, non-symmetrically related carbons defined in (a) and (b), see also Figure S39.

Raman spectroscopy: The precursor PDAs **4a,b** both exhibit strong alkene peaks at 1494 and 1491 cm^{-1}, respectively, as well as alkyne peaks at 2117 and 2120 cm^{-1}, respectively, which are typical of an eneyne backbone (Figure 3d,e, bottom trace). Upon heating, these signals disappear, while the signature D and G peaks of GNRs **1a,b** appear (Figure 3d,e, top traces). The Raman spectra for fjord-edge N_2[8]GNRs **1a,b** show D peaks at 1360 and 1362 cm^{-1}, and G peaks at 1607 and 1608 cm^{-1}, respectively. Relative to a large sheet of graphene, the G peaks of these GNRs are upshifted by ~30 cm^{-1} from graphene (1580 cm^{-1}), due to the confined, strongly aggregated nature of GNRs **1a,b** (see Fig. S32).[51] Prior reports on GNRs show similar shifts in the D peak as well.[53] Furthermore, the broad feature of the observed D peaks can be attributed to the fjord edge structure and the high levels of site-specific heteroatom substitutions, as discussed below.

Broadening of the D peak is generally caused by defects within the graphene lattice.[54,55,56] Bond vacancies, atom vacancies, and heteroatoms distort the lattice away from perfect sp^2 graphitic carbon, which are reflected in the D peak. Fjord-edge GNRs with site-specific nitrogen substitutions have two inherent structural features that broaden the D peak beyond previously reported GNR examples. Specifically, fjord-edges represent bond vacancies along the edges of pristine graphene, which mimic the effect of holey graphene.[57] Broad D and G peaks with higher I_D/I_G ratios indicate large numbers of defects, which characteristically describe holey graphene, and such broadened D peaks can be seen in the all-carbon fjord edge [8]GNR.[27]

Further broadening of the D peaks is caused by nitrogen dopant distortion of the lattice. Reports for both nitrogen doped graphene and top-down synthesized doped GNRs have shown this broadening with various levels of dopant atoms.[58,59] The bottom-up approach of our synthesis incorporates high levels of nitrogen doping, at 12.5%, which most likely further accounts for the broad D peak relative to other examples with under 5% atom doping.[60]

XPS spectra: To confirm the formation of a fjord-edge topology in compounds **1a,b**, we examined the nitrogen bonding environment present in our GNRs using XPS spectroscopy (Figure 4). GNRs **1a,b** should contain solely pyridinic and amide nitrogens if the fjord edge is exclusively formed. Examining the XPS spectra for **1a,b**, they show signatures corresponding to the pyridinic[12,13] (398.7 eV) and amide[61] (399.7 eV) bonding, and no other species (Figure 4). Notably, we do not see the presence of internal graphitic[62,63,64,65] or pyridinium species,[66,67] which would indicate further cyclizations have occurred beyond a fjord edge structure (see discussion below and Figure 6). Additionally, the retention of the sidechain substituents indicates that the alternate path of cyclization to an edge-like topology (**7'a,b**), via intermediates **7a,b** (Figures 5 and 6), does not occur, in agreement with the calculations (see below), which show this pathway to be highly unfavorable. The increased width of the amide peak relative to the pyridinic peak is consistent with conformational disorder in the side-chains only. Together, these results all indicate that the structure most consistent with the data is that in the fjord-edge N_2[8]GNRs **1a,b**.

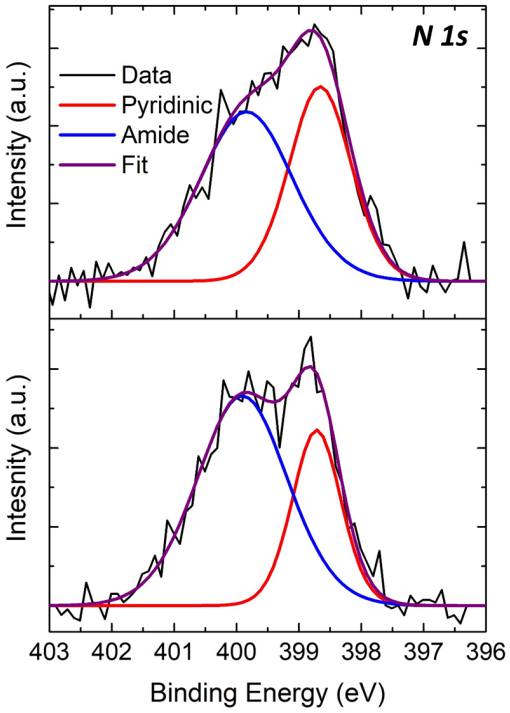

Figure 4. N 1s XPS spectra for fjord-edge N_2[8]GNR **1a** and **1b**, with pyridinic and amide nitrogens centered at 398.7 and 399.7 eV, respectively.

Cyclization pathways and reaction barriers: There are two possible Hopf cyclization pathways for PDAs **4a,b** (Figure 5), which could afford fjord-edge GNRs with two different topologies. The internal-like topology (**1a,b**) would have the nitrogen atoms arranged opposite to a C–H bond on the following "diazachrysene" unit, while the edge-like topology (**7a,b**) would have them at the edges of the nanoribbon. Unlike our previous work on [8]$_A$GNR,[50] which forms the same structure regardless of the initial cyclization pathway at the 4 or 6-positions of the PDAs' phenyl rings, cyclization at either the 4 or 6-position of the pyridyl rings in PDAs **4a,b** could give two different fjord-edge GNRs, or a statistical mixture alternating both pathways along the nanoribbon

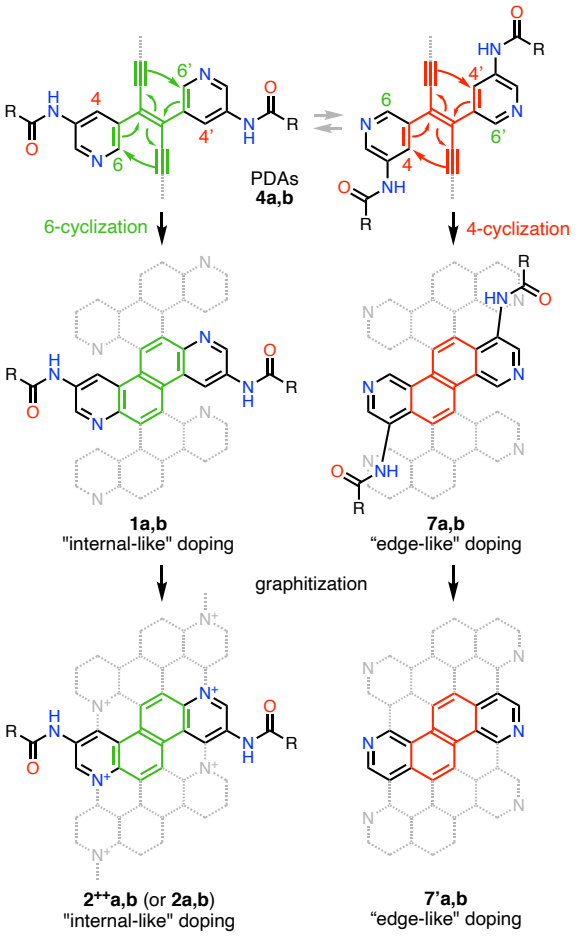

Figure 5. Possible Hopf cyclization pathways for PDAs **4a,b** occurring at either the 4 or 6-positions of the pyridyl rings, leading to nitrogen at "internal" or "edge-like" locations.

length if the difference between reaction barriers is less than 1 kcal·mol^{-1}. However, cyclization at the 4-position should be strongly disfavored owing to the severe steric clash introduced between the amide groups and adjacent pyridyl units during Hopf cyclization (Figure 5, right side). On the other hand, further aromatization to an edge doped armchair GNR should occur easily, resulting in total loss of the sidechains, which is not confirmed by our experimental data. Instead, cyclization at the 6-position produces the lesser strained, internally doped fjord-edge N_2[8]GNRs **1a,b** with their amide sidechains pointing away from the adjacent "diazachrysene" units. The calculations reported below, as well as the XPS data in Figure 4, both strongly support that cyclization has occurred at the 6-pyridyl positions to yield fjord-edge N_2[8]GNRs **1a,b**.

We base our theoretical considerations on previous results by Prall et al.[68] and our own work,[50] which support a Hopf cyclization pathway for this class of systems. The Hopf cyclization proceeds through an initial 6π-electrocyclization, followed by two consecutive [1,2]-H shifts, with the first H-shift as the rate-determining step. The enediyne model system **8** (Figure 6) can undergo cyclization at either the 6-position (*para* to the amide group) or the 4-position (*ortho* to the amide group), the latter of which is likely unfavorable due to the large steric bulk of the amide group, compared to only H in **1a,b**. Using density functional theory (DFT), we computed the geometries of the transition states for the initial

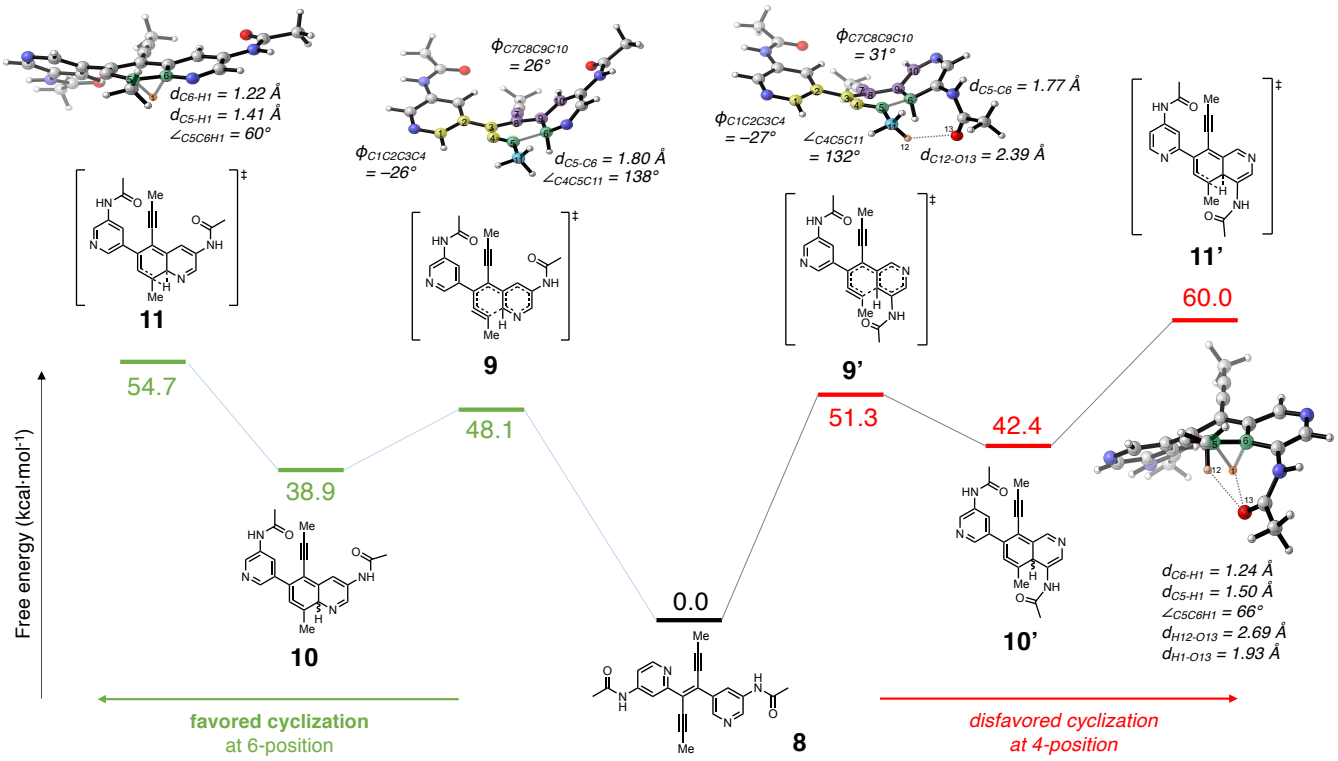

Figure 6. Free energy surface of pathways to desired product (left) and undesired product (right) relative to starting structure **8** (in kcal·mol^{-1}).

6π electrocyclizations (**9** and **9'**), the strained allene intermediates **10** and **10'**, and the transition states for the 1,2-shifts (**11** and **11'**). Structures were optimized in the gas-phase using B3LYP/6-31G(d), and single-point energy calculations were performed using M06-2X/6-311+G(d,p) with B3LYP frequencies to obtain free energy values. The potential energy surfaces for the two cyclization pathways are shown in Figure 6.

The energetic trends for this bispyridyl system are similar to the all-carbon system previously studied by us.[50] As expected, the barriers for *ortho* cyclization are higher than those for *para* cyclization. The activation free energies for the more favorable transition states **9** and **11** are 48.1 and 54.7 kcal·mol^{-1}, respectively, while the analogous transition states **9'** and **11'** have higher barriers of 51.3 and 60.0 kcal·mol^{-1}, respectively. Like the all-carbon PDAs previously studied, the 1,2-shift following electrocyclization is the rate-determining step in both pathways, and the preference for the *para* pathway is substantial (5.3 kcal·mol^{-1}). This energy difference virtually ensures that the analogous series of cyclizations within PDAs **4a,b** should occur exclusively at the 6-positions (*para*) of the pyridyl rings.

The geometries of the transition structures **9** and **9'** are similar to each other and to their all-carbon variants. In **9** and **9'**, the π-system of the alkynes is planar, while the flanking aryl groups are out-of-plane by approximately 30°. The slightly higher barrier of **9'** is likely due to the close proximity of the amide oxygen and methyl group on the forming C–C bond. More differeces can be seen between the rate-determining states **11** and **11'**. In **11**, the quinoline intermediate is planar, and the C6–H1 bond stretches to 1.22 Å from its normal C–H bond length of 1.09 Å. However, in the less-favorable transition state **11'**, the bulky amide group forces the quinoline out of plane, largely due to unfavorable steric interactions between the amide oxygen and the shifting hydrogen and adjacent methyl group, which accounts for the intrinsic preference for the 6-position (*para*) cyclization.

Calculations for the unsubstituted variant (no amide groups) were also computed to probe the intrinsic preference for the 6-position (Figure S35).[51] The barriers of the rate-determining 1,2-shift for the unsubstituted system are 53.7 and 55.7 kcal·mol^{-1} for the 6 and 4-positions, respectively, with only a preference of 2.0 kcal·mol^{-1} for the 6-position. Thus, the increased preference for the 6-position in the substituted system **8** can be wholly attributed to the unfavorable steric interactions between substituents in the rate-determining transition state structure **11'**.

We note that the barrier of the rate-determining step in pyridyl system **8** is ~3 kcal·mol^{-1} lower than that of the all-carbon system, which does not directly correlate with the ~100 °C lower conversion temperature of this N-based system. We acknowledge that while these gas-phase calculations are useful in understanding the intrinsic regioselectivity of this system, they do not account for other interactions that should arise within the full-length PDA systems **4a,b** in the solid state. In particular, the pyridine nitrogens could be the source of additional inter- and intramolecular H-bonding interactions compared to the all-carbon system. This is in part ascertained by the subtle changes in shapes for the methyl signals of PDA **4a** in its CP/MAS solid-state ^{13}C NMR spectra between 25, 300, and 330 °C. At room temperature, the isopropyl methyl groups appear as a double hump, indicating that they are in a different environment. These double humps eventually coalesce to a single signal in the sample prepared at 330 °C, after the Hopf cyclizations have occurred. This is likely the result of changes in inter- and/or intramolecular H-bonding interactions within the PDA solid-state morphology.

Electronic properties of fully cyclized $N_2[8]_AGNR$: In order to better understand the electronic properties of the fully cyclized (graphitic) $N_2[8]_AGNR$ system, we calculated the electronic Density of States (DOS) for the parent systems **1c** and **2c** (Figures 1 and 7) by means of periodic DFT.[51] The DOS of **1c** and **2c**, obtained from the HSE06 functional on the basis of PBE geometries,[69,70] are depicted in Figure 7. As we can see, fjord-edge GNR **1c** is expected to be a semiconductor, with a bandgap of 2.04 eV (Figure 7a). On the other hand, fully cyclized $N_2[8]_AGNR$ **2c** clearly displays metallic behavior, as indicated by the continuous DOS landscape at the Fermi level depicted in Figure 7b. Notice that the HSE06 results are in agreement with the results at the PBE level of theory (Figure S37).[51] Namely, both predict **2c** to be metallic and **1c** to be a semiconductor, although the band gap predicted by PBE is smaller than by HSE06 (1.43 eV *vs* 2.04 eV, respectively), as expected from the DFT delocalization error.[71] Furthermore, bond-equalization of many of the carbon-carbon bonds within the structure of fully fused $N_2[8]_AGNR$ **2c**, unlike those in fjord edge structure **1c** (Figure S38),[51] indicates that $N_2[8]_AGNR$ **2c** has quinoid character, which incites its metallic nature. This fact is in agreement with the charge density at the Fermi level, which exhibits a delocalized π-character (Figure 7b, inset).

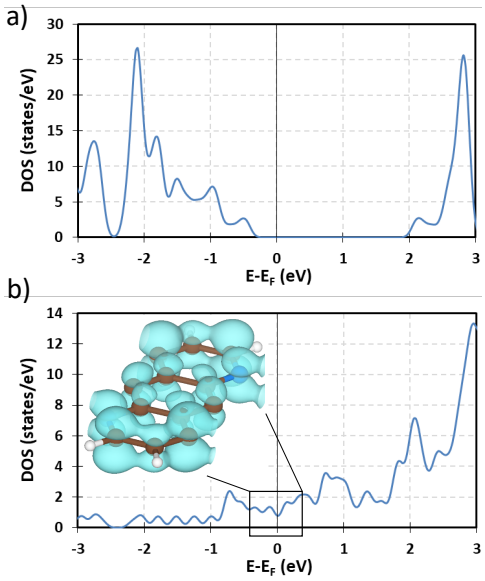

Figure 7. DOS plots calculated at the HSE06 level for a) fjord-edge GNR **1c**, and b) fully cyclized $N_2[8]_AGNR$ **2c**. The inset shows a 3D representation of the partial charge density at the Fermi level in the [–0.2, 0.2] eV range.

These calculations indicate that experimental isolation of the fully cyclized, metallic $N_2[8]_AGNRs$ **2a,b** could be challenging, and despite our best efforts so far, this step is awaiting further work. Formation and characterization of these novel, exciting graphene nanoribbons is currently under investigation.

■ CONCLUSION

In summary, we have demonstrated the synthesis of a novel fjord-edge $N_2[8]GNR$ system with site-specific nitrogen substitution. The stepwise conversion from dipyridyl diynes **3a,b** to the nitrogen doped, fjord edge $N_2[8]GNRs$ **1a,b** via topochemical polymerization of PDAs **4a,b**, followed by Hopf cyclizations to the GNRs proceeded at relatively moderate temperatures of 330-360 °C. The formation of the fjord-edge structure in the GNRs **1a,b** was confirmed via CP/MAS ^{13}C NMR, XPS, and Raman spectroscopy. The success of our bottom-up method demonstrates the versatility of the crystalline state topochemical polymerization method to incorporate heteroatom substitution and structural diversity into GNR structures.

■ ASSOCIATED CONTENT

The Supporting Information is available free of charge at: https://pubs.acs.org/doi/10.1021/jacs.XXXXX.

Experimental procedures and spectroscopic characterization data, crystallization procedures, HR-TEM imaging, and details of the DFT and Molecular Mechanics calculations (PDF).
Crystallographic data (CIF)

■ AUTHOR INFORMATION

Corresponding Author

Yves Rubin – Department of Chemistry and Biochemistry, University of California, Los Angeles, 607 Charles E. Young Dr. East, Los Angeles, California 90095–1567, United States;
orcid.org/ 0000-0003-0187-9689;
Email: rubin@chem.ucla.edu

Notes

The authors declare no competing financial interest.

■ ACKNOWLEDGMENTS

This work was supported by grants from the National Science Foundation to Y.R. (NSF-CHE-1808836), to K.N.H. (NSF-DMR-1335645 and NSF-CHE-1254897), to A.N.A. (NSF-CHE-1351968), to S.H.T. and Y.R. (NSF-CHE-1608957) and NSF-MRI-1532232. This work used computational and storage services associated with the Hoffman2 cluster provided by the UCLA Institute for Digital Research and Education's Research Technology Group, the NSF-supported Extreme Science and Engineering Discovery Environment (XSEDE) (NSF-OCI–1054575 and TG-CHE160054), and high-performance research computing resources by Texas A&M University (http://hprc.tamu.edu). M.D.F. is funded by a Ruth L. Kirschstein National Research Service Award GM007185 and a National Science Foundation Graduate Research Fellowship. C.-T.Z. is funded by a George Gregory Fellowship. R.B.K. thanks the Dr. Myung Ki Hong Chair in Materials Innovation. Data collection at the Argonne National Lab was funded by DOE grant no. DE-FC02-02ER63421. We thank Drs. Duilio Cascio and Michael R. Sawaya for organizing the single crystal data collection at the Advanced Photon Source of Argonne National Laboratory, and Prof. Jose A. Rodriguez for advice and assistance with the crystal data collection and structure analysis.

■ REFERENCES

[1] Zhou, X.; Yu, G. Modified Engineering of Graphene Nanoribbons Prepared via On-Surface Synthesis. *Adv. Mater.* **2019**, 32, 1905957. https://doi.org/10.1002/adma.201905957

[2] Llinas, J. P.; Fairbrother, A.; Barin G. B.; Shi, W.; Lee, K.; Wu,S.; Choi, B. Y.; Braganza, R.; Lear, J.; Kau, N.; Choi, W.; Chen,C.; Pedramrazi, Z.; Dumslaff, T.; Narita, A.; Feng, X.; Müllen, K.; Fischer, F.; Zettl, A.;Ruffieux, P.; Yablonovitch, E.; Crommie, M.; Fasel, R.; Bokor, J. Short-Channel Field-Effect Transistors with 9-Atom and 13-Atom Wide Graphene Nanoribbons. *Nature Commun.* **2017**, *8*, 633. https://doi.org/10.1038/s41467-017-00734-x

[3] Li, X.; Wang, X.; Zhang, L.; Lee, S.; Dai, H. Chemically Derived, Ultrasmooth Graphene Nanoribbon Semiconductors. *Science* **2008**, *319*, 1229–1232. https://doi.org/10.1126/science.1150878

[4] Shen, H.; Shi, Y.; Wang, X. Synthesis, Charge Transport and Device Applications of Graphene Nanoribbons. *Synth. Met.* **2015**, *210*, 109–122. https://doi.org/10.1016/j.synthmet.2015.07.010

[5] Rajaji, U.; Arumugam, R.; Chen, S.-M.; Chen, T.-W.; Tseng, T.-W.; Chinnapaiyan, S.; Lee, S.-Y.; Chang, W.-H. Graphene Nanoribbons in Electrochemical Sensors and Biosensors: A Review. *Int. J. Electrochem. Sci.* **2018**, *13*, 6643-6654. https://doi.org/10.20964/2018.07.51

[6] Cho, K. M.; Cho, S.-Y.; Chong, S.; Koh, H.-J.; Kim, D. W.; Kim, J.; Jung, H.-T. Edge-Functionalized Graphene Nanoribbon Chemical Sensor: Comparison with Carbon Nanotube and Graphene. *ACS Appl. Mater. Interfaces* **2018**, *10*, 42905–42914. https://doi.org/10.1021/acsami.8b16688

[7] Nakada, K.; Fujita, M.; Dresselhaus, G.; Dresselhaus, M. S. Edge State in Graphene Ribbons: Nanometer Size Effect and Edge Shape Dependence. *Phys. Rev. B* **1996**, *54*, 17954-17961. https://doi.org/10.1103/PhysRevB.54.17954

[8] Fujita, M.; Wakabayashi, K.; Nakada, K.; Kusakabe, K. Peculiar Localized State at Zigzag Graphite Edge. *J. Phys. Soc. Jpn.* **1996**, *65*, 1920-1923. https://doi.org/10.1143/JPSJ.65.1920

[9] Hao, Z.; Zhang, H.; Ruan, Z.; Yan, C.; Lu, J.; Cai, J. Tuning Electronic Properties of Atomically Precise Graphene Nanoribbons by Bottom-up Fabrications. *ChemNanoMat* **2020**. https://doi.org/10.1002/cnma.201900706

[10] Wang, X.-Y.; Yao, X.; Müllen, K. Polycyclic Aromatic Hydrocarbons in the Graphene Era. *Sci. China Chem.* **2019**, *62*, 1099–1144. https://doi.org/10.1007/s11426-019-9491-2

[11] Cai, J.; Ruffieux, P.; Jaafar, R.; Bieri, M.; Braun, T.; Blankenburg, S.; Muoth, M.; Seitsonen, A.; Saleh, M.; Feng, X.; Müllen, K.; Fasel, R. Atomically Precise Bottom-up Fabrication of Graphene Nanoribbons. *Nature* **2010**, *466*, 470–473. https://doi.org/10.1038/nature09211

[12] Bronner, C.; Durr, R.A.; Rizzo, D.J.; Lee, Y.-L.; Marangoni, T.; Kalayjian, A. M.; Rodriguez, H.; Zhao, W.; Louie, S. G.; Fischer, F. R.; Crommie, M. F. Hierarchical On-Surface Synthesis of Graphene Nanoribbon Heterojunction. *ACS Nano* **2018**, *12*, 2193-2200. https://doi.org/10.1021/acsnano.7b08658

[13] Beyer, D.; Wang, S.; Pignedoli, C. A.; Melidonie, J.; Yuan, B.; Li, C.; Wilhelm, J.; Ruffieux, P.; Berger, R.; Müllen, K.; Fasel, R.; Feng, X. Graphene Nanoribbons Derived from Zigzag Edge-Encased Poly(para-2,9-dibenzo[bc,kl]coronenylene) Polymer Chains. *J. Am. Chem. Soc.* **2019**, *141*, 2843-2846. https://doi.org/10.1021/jacs.8b10407

[14] Radocea, A.; Sun, T.; Vo, T.; Sinitskii, A.; Aluru, N.; Lyding, J. Solution-Synthesized Chevron Graphene Nanoribbons Exfoliated onto H:Si(100). *Nano Letters* **2016**, *17*, 170–178. https://doi.org/10.1021/acs.nanolett.6b03709

[15] Gao, J.; Uribe-Romo, F. J.; Saathoff, J. D.; Arslan, H.; Crick, C. R.; Hein, S. J.; Itin, B.; Clancy, P.; Dichtel, W. R.; Loo, Y.-L. Ambipolar Transport in Solution-Synthesized Graphene Nanoribbons. *ACS Nano* **2016**, *10*, 4847−4856. https://doi.org/10.1021/acsnano.6b00643

[16] Li, G.; Yoon, K.-Y.; Zhong, X.; Zhu, X.; Dong, G. Efficient Bottom-Up Preparation of Graphene Nanoribbons by Mild Suzuki–Miyaura Polymerization of Simple Triaryl Monomers. *Chem. - Eur. J.* **2016**, *22*, 9116−9120. https://doi.org/10.1002/chem.201602007

[17] Yang, W.; Lucotti, A.; Tommasini, M.; Chalifoux, W. A. Bottom-Up Synthesis of Soluble and Narrow Graphene Nanoribbons Using Alkyne Benzannulations. *J. Am. Chem. Soc.* **2016**, *138*, 9137−9144. https://doi.org/10.1021/jacs.6b03014

[18] Hayashi, H.; Yamaguchi, J.; Jippo, H.; Hayashi, R.; Aratani, N.; Ohfuchi, M.; Sato, S.; Yamada, H. Experimental and Theoretical Investigations of Surface-Assisted Graphene Nanoribbon Synthesis Featuring Carbon-Fluorine Bond Cleavage. *ACS Nano* **2017**, *11*, 6204-6210. https://doi.org/10.1021/acsnano.7b02316

[19] Di Giovannantonio, M.; Deniz, O.; Urgel, J.I.; Widmer, R.; Dienel, T.; Stolz, S.; Sánchez-Sánchez, C.; Muntwiler, M.; Dumslaff, T.; Berger, R.; Narita, A.; Feng, X.; Müllen, K.; Ruffieux, P.; Fasel, R. On-Surface Growth Dynamics of Graphene Nanoribbons: The Role of Halogen Functionalization. *ACS Nano* **2018**, *12*, 74-81. https://doi.org/10.1021/acsnano.7b07077

[20] Ruffieux, P.; Wang, S.; Yang, B.; Sánchez-Sánchez, C.; Liu, J.; Dienel, T.; Talirz, L.; Shinde, P.; Pignedoli, C. A.; Passerone, D.; Dumslaff, T.; Feng, X.; Müllen, K.; Fasel, R. On-Surface Synthesis of Graphene Nanoribbons with Zigzag Edge Topology. *Nature* **2016**, *531*, 489-492. https://doi.org/10.1038/nature17151

[21] Lee, Y-L.; Zhao, F.; Cao, T.; Ihm, J.; Louie, S. G. Topological Phases in Cove-Edged and Chevron Graphene Nanoribbons: Geometric Structures, z_2 Invariants, and Junction States. *Nano Lett.* **2018**, *18*, 7247-7253. https://doi.org/10.1021/acs.nanolett.8b03416

[22] Teeter, J. D.; Costa, P. S.; Pour, M. M.; Miller, D. P.; Zurek, E.; Enders, A.; Sinitskii, A. Epitaxial Growth of Aligned Atomically Precise Chevron Graphene Nanoribbons on Cu(111). *Chem. Commun.* **2017**, *53*, 8463-8466. https://doi.org/10.1039/C6CC08006E

[23] Bronner, C.; Stremlau, S.; Gille, M.; Braußе, F.; Haase, A.; Hecht, S.; Tegeder, P. Aligning the Band Gap of Graphene Nanoribbons by Monomer Doping. *Angew. Chem. Int. Ed.* **2013**, *52*, 4422–4425. https://doi.org/10.1002/anie.201209735

[24] Liu, J.; Li, B.-W.; Tan, Y.-Z.; Giannakopoulos, A.; Sánchez-Sánchez, C.; Belijonne, C.; Ruffieux, P.; Fasel, R.; Feng, X.; Müllen, K. Toward Cove-Edged Low Band Gap Graphene Nanoribbons. *J. Am. Chem. Soc.* **2015**, *137*, 6097-6103. https://doi.org/10.1021/jacs.5b03017

[25] Verzhbitskiy, I. A.; De Corato, M.; Ruini, A.; Molinari, E.; Narita, A.; Hu, Y.; Schwab, M. G.; Bruna, M.; Yoon, D.; Milana, S.; Feng, X.; Müllen, K.; Ferrari, A. C.; Casiraghi, C.; Prezzi, D. Raman Fingerprints of Atomically Precise Graphene Nanoribbons. *Nano Lett.* **2016**, *16*, 3442-3447. https://doi.org/10.1021/acs.nanolett.5b04183

[26] Wu, J.; Gu, Y.; Muñoz-Mármol, R.; Wu, S.; Han, Y.; Ni, Y.; Díaz-García, M.; Casado, J. Cove-Edged Nanographenes with Localized Double Bonds. *Angew. Chem. Int. Ed.* **2020**. https://doi.org/10.1002/anie.202000326

[27] Yano, Y.; Mitoma, N.; Matsushima, K.; Wang, F.; Matsui, K.; Takakura, A.; Miyauchi, Y.; Ito, H.; [27], K. Living Annulative π-Extension Polymerization for Graphene Nanoribbon Synthesis. *Nature* **2019**, *571*, 387-392. https://doi.org/10.1038/s41586-019-1331-z

[28] Moreno, C.; Vilas-Varela, M.; Kretz, B.; Garcia-Lekue, A.; Costache, M. V.; Paradinas, M.; Panighel, M.; Ceballos, G.; Valenzuela, S. O.; Peña, D.; Mugarza, A. Bottom-up Synthesis of Multifunctional Nanoporous Graphene. **2018**, *360*, 199–203. https://doi.org/10.1126/science.aar2009

[29] Pawlak, R.; Liu, X.; Ninova, S.; D'Astolfo, P.; Drechsel, C.; Sangtarash, S.; Häner, R.; Decurtins, S.; Sadeghi, H.; Lambert, C. J.; Aschauer, U.; Liu, S.-X.; Meyer, E. Bottom-up Synthesis of Nitrogen-Doped Porous Graphene Nanoribbons. *J. Am. Chem. Soc.* Article ASAP. DOI: 10.1021/jacs.0c03946. https://pubs.acs.org/doi/10.1021/jacs.0c03946

[30] Peter H. Jacobsen, Ryan D. McCurdy, Jingwei Jiang, Daniel J. Rizzo, Gregory Veber, Paul Butler, Rafal Zuzak, Steven G. Louie, Felix R. Fischer, and Michael F. Crommie, Bottom-up Assembly of Nanoporous Graphene with Emergent Electronic States, *J. Am. Chem. Soc.* **2020**, Just Accepted Manuscript. https://doi.org/10.1021/jacs.0c05235

[31] Wang, X.-Y.; Yao, X.; Narita, A.; Müllen, K. Heteroatom-Doped Nanographenes with Structural Precision. *Acc. Chem. Res.* **2019**, *52*, 2491-2505. https://doi.org/10.1021/acs.accounts.9b00322

[32] Kawai, S.; Saito, S.; Osumi, S.; Yamaguchi, S.; Foster, A. S.; Spijker, P.; Meyer, E. Atomically Controlled Substitutional Boron-Doping of Graphene Nanoribbons. *Nature Commun.* **2015**, *6*, 8098. https://doi.org/10.1038/ncomms9098

[33] Wang, X.-Y.; Urgel, J. I.; Barin, G. B.; Eimre, K.; Di Giovannantonio, M.; Milani, A.; Tommasini, M.; Pignedoli, C. A.; Ruffieux, P.; Feng, X.; Fasel, R.; Müllen, K.; Narita, A. Bottom-Up Synthesis of Heteroatom-Doped Chiral Graphene Nanoribbons. *J. Am. Chem. Soc.* **2018**, *140*, 9104-9107. https://doi.org/10.1021/jacs.8b06210

[34] Cao, Y.; Qi, J.; Zhang, Y.-F.; Huang, L.; Zheng, Q.; Lin, X.; Cheng, Z.; Zhang, Y.-Y.; Feng, X.; Du, S.; Pantelides, S.T.; Gao, H.-J. Tuning the Morphology of Chevron-Type Graphene Nanoribbons by Choice of Annealing Temperature. *Nano Research* **2018**, *11*, 6190-6196. https://doi.org/10.1007/s12284-018-2136-3

[35] Nguyen, G.D.; Toma, F. M.; Cao, T.; Pedramrazi, Z.; Chen, C.; Rizzo, D. J.; Joshi, T.; Bronner, C.; Chen, Y.-C.; Favaro, M.; Louie, S. G.; Fischer, F. R.; Crommie, M. F. Bottom-Up Synthesis of N=13 Sulfur-Doped Graphene Nanoribbons. *J. Phys. Chem. C* **2016**, *120*, 2684-2687. https://doi.org/10.1021/acs.jpcc.5b09986

[36] Kim, K. T.; Lee, J. W.; Jo, W. H. Charge-Transport Tuning of Solution-Processable Graphene Nanoribbons by Substitutional Nitrogen Doping. *Macromol. Chem. Phys.* **2013**, *214*, 2768-2773. https://doi.org/10.1002/macp.201300529

[37] Vo, T. H.; Perera, U. G. E.; Shekhirev, M.; Pour, M. M.;Kunkel, D.A.; Lu, H.; Gruberman, A.; Sutter, E.; Cotlet, M.; Nykypanchuk, D.; Zahl, P.; Enders,A.; Sinitskii, A.; Sutter, P. Nitrogen-Doping Induced Self-Assembly of Graphene Nanoribbon-Based Two-Dimensional and Three-Dimensional Metamaterials. *Nano Lett.* **2015**, *15*, 5770-5777. https://doi.org/10.1021/acs.nanolett.5b01723

[38] Kawai, S.; Nakatsuka, S.; Hatakeyama, T.; Pawlak, R.; Meier, T.; Tracey, J.; Meyer, E.; Foster, A. S. Multiple Heteroatom Substitution to Graphene Nanoribbon. *Science Advances* **2018**, *4*, eaar7181. https://doi.org/10.1126/sciadv.aar7181

[39] Cloke, R. R.; Marangoni, T.; Nguyen, G. D.; Joshi, T.; Rizzo, D. J.; Bronner, C.; Cao, T.; Louie, S. G.; Crommie, M. F.; Fischer, F. R. Site-Specific Substitutional Boron Doping of Semiconducting Armchair Graphene Nanoribbons. *J. Am. Chem. Soc.* **2015**, *137*, 8872–8875. https://doi.org/10.1021/jacs.5b02523

[40] Piskun, I.; Blackwell, R.; Jornet-Somoza, J.; Zhao, F.; Rubio, A.; Louie, S.; Fischer, F. Covalent C-N Bond Formation through a Surface Catalyzed Thermal Cyclodehydrogenation. *J. Am. Chem. Soc.* **2020**, *142*, 3696-3700 . https://doi.org/10.1021/jacs.9b13507

[41] Cai, J.; Pignedoli, C. A.; Talirz, L.; Ruffieux, P.; Sode, H.; Liang, L.; Meunier, V.; Berger, R.; Li, R.; Feng, X.; Müllen, K.; Fasel, R. Graphene Nanoribbon Heterojunctions. *Nat. Nanotechnol.* **2014**, 9, 896–900. https://doi.org/10.1038/nnano.2014.184

[42] Zhang, Y.; Zhang, Y.; Li, G.; Lu, J.; Lin, X.; Du, S.; Berger, R.; Feng, X.; Müllen, K.; Gao, H.-J. Direct Visualization of Atomically Precise Nitrogen-Doped Graphene Nanoribbons. *Appl. Phys. Lett.* **2014**, 105, 023101. https://doi.org/10.1063/1.4884359

[43] Durr, R. A.; Haberer, D.; Lee, Y.-L.; Blackwell, R.; Kalayjian, A. M.; Marangoni, T.; Ihm, J.; Louie, S. G.; Fischer, F. R. Orbitally Matched Edge-Doping in Graphene Nanoribbons. *J. Am. Chem. Soc.* **2018**, *140*, 807-813. https://doi.org/10.1021/jacs.7b11886

[44] Vo, T. H.; Shekhirev, M.; Kunkel, D. A.; Orange, F.; Guinel, M. F.-F.; Enders, A.; Sinitskii, A. Bottom-Up Solution Synthesis of Narrow Nitrogen-Doped Graphene Nanoribbons. *Chem. Commun.* **2014**, *50*, 4172-4174. https://doi.org/10.1039/C4CC00885E

[45] Kolmer, M.; Steiner, A. K.; Izydorczyk, I.; Ko, W.; Engelund, M. Szymonski, M.; Amsharov, K. Rational Synthesis of Atomically Precise Graphene Nanoribbons Directly on Metal Oxide Surfaces. *Science* 10.1126/science.abb8880 (2020).

[46] Wegner, G. Topochemical Polymerization of Monomers with Conjugated Triple Bonds. *Makromol. Chem.* **1972**, *154*, 35-48. https://doi.org/10.1002/mcap.1972.021540103

[47] Enkelmann V. (1984) Structural aspects of the topochemical polymerization of diacetylenes. In: Cantow HJ. (eds)

Polydiacetylenes. Advances in Polymer Science, vol 63. Springer, Berlin, Heidelberg. https://doi.org/10.1007/BFb001765

[48] Lauher, J.; Fowler, F.; Goroff, N. Single-Crystal-to-Single-Crystal Topochemical Polymerizations by Design. *Accounts of Chemical Research* **2008**, *41*, 1215–1229. https://doi.org/10.1021/ar8001427

[49] Jordan, R. S.; Wang, Y.; McCurdy, R. D.; Yeung, M. T.; Marsh, K. L.; Kahn, S. I.; Kaner, R. B.; Rubin, Y. Synthesis of Graphene Nanoribbons via the Topochemical Polymerization and Subsequent Aromatization of a Diacetylene Precursor. *Chem* **2016,** *1*, 78-90. https://doi.org/10.1016/j.chempr.2016.06.010

[50] Jordan, R. S.; Li, Y. L.; Lin, C-W.; McCurdy, R. D.; Lin, J. B.; Brosmer, J. L.; Marsh, K. L.; Khan, S. I.; Houk, K. N.; Kaner, R. B.; Rubin, Y. Synthesis of *N* = 8 Armchair Graphene Nanoribbons from Four Distinct Polydiacetylenes. *J. Am. Chem. Soc.* **2017**, *139*, 15878-15890. https://doi.org/10.1021/jacs.7b08800

[51] See Supporting Information.

[52] See reference 47 for a similar observation on an intermediate stage to $[8]_A$GNR.

[53] Ryu, S.; Maultzsch, J.; Han, M. Y.; Kim, P.; Brus, L. E. Raman Spectroscopy of Lithographically Patterned Graphene Nanoribbons. *ACS Nano* **2011**, *5*, 4123−4130. https://doi.org/10.1021/nn200799y

[54] Ortiz-Medina, J.; García-Betancourt, M. L.; Jia, X.; Martínez-Gordillo, R.; Pelagio-Flores, M. A.; Swandon, D.; Elías, A.L. Gutiérrez, H. R. ; Garcia-Espino, E.; Meunier, V.; Owens, J.; Sumpter, B.G.; Cruz-Silva, E.; Rodríguez-Macías, F.J.; López-Urías, F.; Muñoz-Sandoval, E.; Dresselhaus, M. S.; Terrones, H.; Terrones, M. Nitrogen-Doped Graphitic Nanoribbons:Synthesis, Characterization, and Transport. *Adv. Funct. Mater.* **2013**, *23*, 3755-3762. https://doi.org/10.1002/adfm.201202947

[55] Daigle, M.; Maio, D.; Lucotti, A.; Tommasini, M.; Morin, J.-F. Helically Coiled Graphene Nanoribbons. *Angew. Chem.* **2017**, *129*, 6309-6313. https://doi.org/10.1002/ange.201611834

[56] Zhang, C.; Fu, L.; Liu, N.; Lui, M.; Wang, Y.; Liu, Z. Synthesis of Nitrogen-Doped Graphene Using Embedded Carbon and Nitrogen Sources. *Adv. Mater.* **2011**, *23*, 1020-1024. https://doi.org/10.1002/adma.201004110

[57] Hu, X.; Bai, D.; Wu, Y.; Chen, S.; Ma, Y.; Lu, Y.; Chao, Y.; Bai, Y. A Facile Synthesis of Reduced Holey Graphene Oxide for Supercapacitors. *Chem. Commun.* **2017**, *53*, 13225-13228. https://doi.org/10.1039/C7CC07475A

[58] Lu, Y.-F.; Lo, S.-T.; Lin, J.-C.; Zhang, W.; Lu, J.-Y.; Liu, F.-H.; Tseng, C.-M.; Lee, Y.-H.; Liang, C.-T.; Li, L-L. Nitrogen-Doped Graphene Sheets Grown by Chemical Vapor Deposition : Synthesis and Influence of Notrogen Impurities on Carrier Transport. *ACS Nano* **2013**, *7*, 6522-6532. https://doi.org/10.1021/nn402102y

[59] Liu, M.; Song, Y.; He, S.; Tjiu, W. W.; Pan, J.; Xia, Y.-Y.; Liu, T. Nitrogen-Doped Graphene Nanoribbons as Efficient Metal-Free Electrocatalysts for Oxygen Reduction. *ACS Appl. Mater. Interfaces* **2014**, *6*, 4212-4222. https://doi.org/10.1021/am405900r

[60] Wang, G.; Maiyalagan, T.; Wang, X. Review on Recent Progress in Nitrogen-Doped Graphene: Synthesis, Characterization, and Its Potential Applications. *ACS Catal.* **2012**, *2*, 781-794. https://doi.org/10.1021/cs200652y

[61] Jansen, R. J. J.; van Bekkum, H. XPS of Nitrogen-Containing Functional Groups on Activated Carbon. *Carbon* **1995**, *8*, 1021-1027. https://doi.org/10.1016/0008-6223(95)00030-H

[62] Tian, Z.; Dai, S.; Jiang, D. Stability and Core-Level Signature of Nitrogen Dopants in Carbonaceous Materials. *Chem. Mater.* **2015**, *27*, 5775-5781. https://doi.org/10.1021/acs.chemmater.5b02370

[63] Kapteijn, F.; Moulijn, J.A.; Matzner, S.; Boehm H.-P. The Development of Nitrogen Functionality in Model Chars during Gasification in CO_2 and O_2. *Carbon,* **1999**, *37*, 1143-1150. https://doi.org/10.1016/500008-6223(98)00312-1

[64] Geng, J.; Si, L.; Guo, H.; Lin, C.; Xi, Y.; Li, Y.; Yan, X.; Wang, B.; Chen, L. 3D Nitrogen-Doped Graphene Gels as Robust and Sustainable Adsorbents for Dyes. *New J. Chem.* **2017**, *41*, 15447-15457. https://doi/org/10.1039/C7NJ02984E

[65] Kondo, T.; Casolo, S.; Suzuki, T.; Shikano, T.; Sakurai, M.; Harada, Y.; Saito, M.; Oshima, M.; Trioni, M. I.; Tantardini, G. F.; Nakamura, J. Atomic-Scale Characterization of Nitrogen-Doped Graphite: Effects of Dopant Nitrogen on the Local Electronic Structure of the Surrounding Carbon Atoms. *Phys. Rev. B* **2012**, *86*, 035436. https://doi.org/10.1103/PhysRevB.86.035436

[66] Matanovic, I.; Artyushkova, K.; Strand, M. B.; Dzara, M. J.; Pylypenko, S.; Atanassov, P. Core Level Shifts of Hydrogenated Pyridinic and Pyrrolic Nitrogen in the Nitrogen-Containing Graphene-Based Electrocatalysts: In-Place vs Edge Defects. *J. Phys. Chem. C* **2016**, *120*, 29225-29232. https://doi.org/10.1021/acs.jpcc.6b09778

[67] Men, S.; Mitchell, D. S.; Lovelock, K. R. J.; License P. X-ray Photoelectron Spectroscopy of Pyridinium-Based Ionic Liquids: Comparison to Imidazolium- and Pyrrolidinium-Based Analogues. *ChemPhysChem* **2015**, *16*, 2211-2218. https://doi.org/10.1002/cphc.201500227

[68] Prall, M.; Krüger, A.; Schreiner,P. R.; Hopf, H. The Cyclization of Parent and Cyclic Hexa-1,3-dien-5-ynes—A Combined Theoretical and Experimental Study. *Chem. Eur. J.* **2001**, *7*, 4386-4394. https://doi.org/10.1002/1521-3765(20011015)7:20<4386::AID-CHEM4386>3.0CO;2-S

[69] Perdew, J. P.; Burke, K.; Ernzerhof, M. Generalized Gradient Approximation Made Simple. *Phys. Rev. Lett.* **1996**, *77*, 3865−3868. https://doi.org/10.1103/PhysRevLett.77.3865

[70] Krukau, A. V.; Vydrov, O. A.; Izmaylov, A. F.; Scuseria, G. E. Influence of the exchange screening parameter on the performance of screened hybrid functionals. *J. Chem. Phys.* **2006**, *125*, 224106. https://doi.org/10.1063/1.2404663

[71] Mori-Sanchez, P.; Cohen, A. J.; Yang, W. Localization and Delocalization Errors in Density Functional Theory and Implications for Band-Gap Prediction. *Phys. Rev. Lett.* **2008**, *100*, 146401. https://doi.org/10.1103/PhysRevLett.100.146401